Functional macroporous iron-phosphorous films by electrodeposition on colloidal crystal templates

Irati Golvano-Escobal[a], Roger de Paz-Castany[a], Carlos Alcantara[b], Salvador Pané[b], Eva García-Lecina[c], Jordi Sort[a,d], Eva Pellicer[a]

[a] *Departament de Física, Universitat Autònoma de Barcelona, E-08193 Bellaterra (Cerdanyola del Vallès), Spain*
[b] *Multi-Scale Robotics Lab (MSRL), Institute of Robotics and Intelligent Systems (IRIS), ETH Zurich, CH-8092 Zurich, Switzerland*
[c] *CIDETEC, Paseo Miramón 196, E-20014 Donostia-San Sebastián, Spain*
[d] *Institució Catalana de Recerca i Estudis Avançats (ICREA), Pg. Lluís Companys 23, E-08010 Barcelona, Spain*

Abstract

Pseudo-ordered macroporous iron-phosphorous (Fe-P) films have been electrodeposited potentiostatically from a citrate-sulfate bath onto Au surfaces prepatterned with a colloidal crystal mask of polystyrene spheres of 350 nm in diameter. The electrolyte contained sodium hypophosphite as the P source, enabling the incorporation of 6-14 at.% P. For comparative purposes, continuous films have been obtained galvanostatically on unpatterned Au surfaces. In both cases, the P content could be varied to a certain extent by adjusting the deposition potential or current density. Tunable microstructure and magnetic response was observed due to the dissimilar chemical composition, with coercivity values being larger in the macroporous films. Additionally, wettability analyses showed that these were more hydrophobic, reaching contact angle values of about 130°. In spite of their hydrophobic character, the samples were catalytic toward oxygen evolution reaction (OER) in alkaline media. The macroporous Fe-P films showed faster kinetics for OER than their nonporous counterparts. Our results show that electrodeposited porous Fe-P based materials show an interesting combination of properties which make them appealing for applications includ-

*Corresponding authors:
URL: Jordi.Sort@uab.cat (Jordi Sort), Eva.Pellicer@uab.cat (Eva Pellicer)

ing water cleaning, soft-magnetic components, or electrocatalytic production of oxygen, to name a few.

Keywords: Electrodeposition, iron-phosphorous, macroporous films, wettability, magnetic properties

1. Introduction

The electrodeposition of iron and some of their alloys is not straightforward from aqueous solution due to the oxidation from Fe(II) to Fe(III) at the anode or the precipitation of iron hydroxides at the cathodic surface due to local alkalization [1, 2]. Yet, high quality iron deposits can be obtained from ferrous chloride and calcium chloride (known as Fischer-Langbein) solutions or mixed sulfate-chloride baths, as reviewed by Izaki [3]. Although Fe electrodeposition is complex and, hence, research in this area has been limited, the plating community has recently renewed interests toward Fe plating [4]. Iron is one of the most abundant metals on the Earth's crust, and consequently, a cheaper, and sometimes also a greener, alternative to other metals. Compared to pure Fe, electrodeposition of Fe alloys has been researched more extensively (e.g. alloys with Ni [5], Cu [6], W [2] or metalloids like B [7, 8] or P [9]), often while trying to preserve the features brought by Fe element (ferromagnetism and malleability, among others).

Electrodeposition offers the possibility to produce non-equilibrium alloys in the as-prepared state, which is very interesting when amorphous materials are pursued. In addition, little changes in the growth conditions can result in a significant change in the phase structure of electrodeposits with the same chemical composition [10]. Interestingly, Fe-P with ca. 20 at.% belongs to a group of amorphous alloys that can be obtained by electrochemical means under relatively simple experimental conditions [11].

Fe-P alloys have attracted the interest of researchers because of their magnetic and protective properties which highly depend on the amount of P. The electrodeposition of Fe-P alloy coatings suitable for various purposes like cor-

rosion protection [12], electrical power equipment (transformers, rotating machines, etc.) [13] or electrocatalysis [14] has been explored by several researchers. In particular, Fe-P has been advocated as an outstanding soft magnetic material due to its low coercivity and high magnetic flux density [15]. Particular emphasis has been laid in the production of amorphous films. The impact of pH, current density and glycine concentration on Fe-P electrodeposition from a sulphate electrolyte were explored by Vitkova et al. to find out the optimal conditions toward amorphous films [11]. Likewise, Kamei and Maehara characterized the magnetic properties and the microstructure of electroplated amorphous Fe-P alloys. The authors concluded that the coatings became amorphous for P contents of about 20 at.% or higher [16]. Upon annealing of the as-deposited Fe-P materials, different metal phosphides like Fe_3P, Fe_2P, FeP, and FeP_2 can form [17, 18].

Materials with spatially ordered porous features at the macro- and mesoscales have been explored over the last years. Owing to the synergies arising from their constituent elements, sophisticated shape, and large surface-to-volume ratio (S/V), these materials are advantageous for a wide variety of applications. Photonic devices, catalysis, separation technology, nano-electronics, sensors, batteries, supercapacitors, fuel cells, sorption, thermal insulation, surfaces with special wetting properties, are just some of the myriad applications of porous materials. Although several methods toward periodic porous structures are available, deposition of the material over a colloidal crystal template followed by the selective removal of the latter is attractive for several reasons [19]. Namely, different pore sizes can be targeted by simply changing the diameter of the colloidal particles, layering can be tuned on demand, from thin films to three-dimensionally ordered macroporous materials, and both metals and metal oxides can be produced. The approach encompasses the following steps: (1) the preparation of a colloidal dispersion, (2) the anchorage of the fine particles (typically uniformly sized spheres) onto a substrate by dip-coating, spin-coating, or electrophoretic deposition, (3) the filling of the empty space between the close-packed spheres with the target material, and (4) the selective removal of the

colloidal particles, which can be accomplished by their dissolution in an organic solvent or calcination. As a result, the inverse replica of the parent colloidal crystal template is obtained. Several routes have been employed to date to fill the voids between the beads, namely, sol-gel, emulsion-gel, or liquid phase reaction [20, 21, 22]. Electrodeposition has also been employed to fill the interstitial space between the particles with great success [23]. Compared to other methods, it offers a good control over the degree of filling and wall thickness. Most importantly, many metals can be deposited and co-deposited from the same electrolyte with the possibility of fine-tuning their atomic ratio by simply adjusting the electrochemical parameters [24, 25]. For bead sizes (and, in turn, pore sizes) greater than 50 nm, the resulting films are commonly termed *macroporous*.

Intense research is being carried out during the last few years on porous magnetic materials. Porous films can be used, for example, to achieve enhanced magnetoelectric effects (that is, to induce changes in their magnetic properties by means of externally applied voltages) [26, 27, 28]. Magnetoelectric effects (in particular, voltage-driven reduction of coercivity) can drastically decrease the energy consumption of magnetic storage systems and other types of magnetoelectric devices (because then magnetic switching requires of lower magnetic fields). The large S/V ratio of magnetic porous alloys promotes an enhanced electric surface charging and concomitantly triggers larger magnetoelectric effects [27]. Porous magnetic materials can be also functionalized and effectively charged with drugs, offering the possibility of magnetically-guided drug delivery for anticancer treatments [29]. Also, biodegradability is enhanced in porous materials compared to their bulk counterparts, which can be advantageous for temporary implant devices. In this context, Fe-P foams have been proposed as biodegradable bone replacement materials [30]. Herein, porosity is introduced in order to decrease the Young's modulus of the material to make it closer to bone and increase biodegradability.

The electrolysis of water provides a sustainable and environmentally-friendly way to contribute towards the constantly growing demand for energy supply and

storage. However, the production of H_2 is constrained by the sluggish kinetics of the oxygen evolution reaction (OER) at the anode side of a water electrolyzer [31, 32]. For this reason, huge efforts are devoted to develop low cost electrocatalysts with high activity towards OER. RuO_2 and IrO_2 are the benchmark catalysts for OER [33] but they are costly and their supply is not sustainable [34, 35, 36]. Therefore, the production of more efficient and cheap OER catalysts remains an ongoing challenge. During the last years, transition metal phosphides have attracted the interest of the scientific community for their outstanding catalytic activity towards HER [37, 38, 39, 40]. More recently, they have also been highlighted as catalysts for OER [41, 42]. The OER mechanism of metal phosphide compounds is not completely understood although the formation of oxides and oxyhydroxides (like FeOOH in the case of Fe-P) at their surface is thought to be responsible for the high catalytic activity [43, 44]. The oxidation of phosphides to phosphates during the OER tests has also been claimed to contribute to the OER activity [45]. Typically, iron phosphides show less catalytic activity than their nickel and cobalt analogues [46]. An increase of the catalyst surface area has been demonstrated to remarkably increase the OER performance [47].

Although the influence of various electrodeposition parameters such as the deposition mode (direct current *vs* pulse plating), time, pH and bath temperature on the composition and structure of Fe-P films has been investigated to some extent, such studies dealt with continuous films on planar substrates and nanowires [18, 48]. The electrosynthesis of Fe-P pseudo-ordered porous films remains mostly unexplored. Herein we report on the synthesis of macroporous Fe-P films by electrodeposition through colloidal crystal templates. Special emphasis is laid on ensuring the growth of high-quality porous films with tunable phosphorous content and, in turn, magnetic properties. Alongside, continuous (also named *dense* for the sake of clarity) Fe-P films directly electrodeposited on an unpatterned electrode were produced for comparative purposes. Surface polarity was investigated as well and an increase of the contact angle value was clearly observed in the macroporous coatings irrespective of the Fe/P ratio. In

spite of their enhanced hydrophobic character, the porous films showed higher activity toward oxygen evolution reaction (OER) in alkaline media.

2. Experimental section

2.1. Electrochemical synthesis

Electrodeposition was conducted in a double-jacketed three-electrode cell connected to a PGSTAT302N Autolab potentiostat/galvanostat (Ecochemie). A double junction Ag—AgCl (E=+0.210 V/SHE) reference electrode (Metrohm AG) was used with 3M KCl inner solution and 1M Na_2SO_4 outer solution. A platinum spiral served as a counter electrode. To prepare the continuous films, silicon (111) substrates with e-beam evaporated Ti (10 nm)/Au (90 nm) adhesion/seed layers were used as cathodes. In the case of macroporous films, Si/Ti/Au substrates patterned by colloidal lithography with carboxylated polystyrene (PS) spheres of 350 nm in diameter (purchased from Polysciences) were used. The spheres were electrophoretically deposited on the substrate in a custom-made cell consisting of a chamber (1 cm x 1 cm x 0.6 cm) of poly(methyl methacrylate) (PMMA) glued to a counter electrode of platinized titanium. The Au-coated substrate (anode) was fixed at a distance of 0.5 cm from the counter electrode (cathode). A constant potential was then applied between the anode and the cathode using an Agilent B2902A power source. An electric field of 120 V cm^{-1} was applied during 5 min. Immediately after the electrophoretic deposition, the samples were dried on a hot plate at 50 °C for 10 min.

Several electrolyte formulations were screened for the deposition of good quality Fe-P films on Si/Ti/Au substrates. $FeSO_4 \cdot 7H_2O$ salt was selected as the Fe source and its concentration was kept at 1 M, whereas $NaH_2PO_2 \cdot H_2O$ was chosen as the P source and its concentration was varied between 0.01 M and 0.5 M. The electrolytes also contained citric acid (0.1-0.5 M), $(NH_4)_2\ SO_4$ (0.1 M) and ascorbic acid (0.05 M) to prevent the oxidation of Fe(II) to Fe(III). The pH of the as-prepared electrolytes ranged from pH = 2.0 to pH = 2.5 for the different electrolytes and was kept unadjusted. The Fe/P ratio in the coatings

did not considerably vary upon changing the [Fe(II)]/[$H_2PO_2{}^{-1}$] in solution at a given current density nor with electrolyte temperature (25 °C - 32 °C). For this reason the bath employed in subsequent experiments was 1 M $FeSO_4 \cdot 7H_2O$, 0.5 M $NaH_2PO_2 \cdot H_2O$, 0.1 M citric acid, 0.1 M $(NH_4)_2\ SO_4$ and 0.005 M ascorbic acid, which is similar to that reported by Chandrasekar and Mitra [17]. The pH of the optimized formulation was 2.0 and it was kept unadjusted for the electrodeposition experiments. Solutions were prepared from analytical grade reagents and Milli-Q (MQ)-water. Before each deposition, the electrolyte was de-aerated with nitrogen gas. Deposition was conducted galvanostatically in the case of the dense films and potentiostatically in the case of the porous films. A constant current density between -10 and -50 mA cm^{-2} or a constant potential in the range from -0.96 to -1.1 V were applied, respectively. All deposition processes were carried out at 32 °C under stagnant conditions. The temperature was maintained by circulating water through the external jacket of the electrochemical cell using a refrigerated/heated circulator from Julabo (F12 model). After deposition, the samples were rinsed with MQ-water and dried in air. The PS spheres were selectively etched away by ultrasonication for 4 min in dimethyl sulfoxide (DMSO), followed by 4 min in dimethylformamide (DMF) and finally 15 min in $CHCl_3$. The resulting porous films where thoroughly rinsed in MQ-water again. Pure macroporous Fe films were synthesized from a different electrolyte containing 0.2 M $FeSO_4 \cdot 7H_2O$, 0.1 M glycine and 0.0028 M ascorbic acid (left at its unadjusted pH). The current efficiency of Fe-P deposition was estimated by comparing the actual weight of material deposited, which was determined by inductively coupled plasma optical emission spectrometry (ICP-OES) analyses, with the Faraday's law of electrolysis. Prior to ICP-OES analyses, samples were fully dissolved in 6 wt.% HNO_3. From these, an aliquot of 3 mL was analyzed on a Perkin-Elmer Optima 4300DV spectrometer to determine the concentration of Fe and P in the resulting solutions.

To prepare the Si/Ti/Au substrates, a 4-inch Si wafer was loaded into a commercial e-beam evaporation system (Plassys-II MEB550SL) installed in a cleanroom environment. While in the vacuum chamber, the substrates were

plasma-treated to remove organic contaminants. Immediately after, a 10 nm Ti seed layer was evaporated at a rate of 0.1 nm s^{-1} to act as a buffer interface between the native oxide layer present in the silicon surface and a 90 nm Au thin film, which was evaporated at a rate of 0.5 nm s^{-1}. During e-beam evaporation, the substrate holder was rotated at 4 RPM to increase the homogeneity of the surface. To protect the Ti/Au (10/90 nm)-coated Si wafers during the dicing step, a thin positive-tone photoresist layer (AZ9260, Microchemicals GmbH) was spin-coated at 3000 RPM for 60s, followed by a soft-bake at 100 °C for 60s. Finally, the wafer was diced into smaller chips and cleaned with acetone, isopropyl alcohol and MQ-water immediately prior to electrodeposition.

2.2. Characterization

The morphology and composition of the dense and macroporous Fe-P films were characterized on a Zeiss Merlin field emission scanning electron microscope (FE-SEM) equipped with an energy dispersive X-ray (EDX) detector. Room temperature hysteresis loops were recorded using a vibrating sample magnetometer (VSM) from MicroSense (LOT-Quantum Design), with a maximum applied magnetic field of 2 T applied in-plane. Normalized hysteresis loops by the total Fe and P weights, as determined by ICP-OES, are reported. A surface analyzer (Smartdrop, Femtofab) was used to study the wetting properties of the films (sessile drop technique). The liquid utilized in the measurements was 1 μL droplets of MQ-water at room temperature. The reported contact angle values correspond to the average of two independent measurements. X-ray diffraction (XRD) patterns were recorded on a Philips X'Pert diffractometer in the 25-90° 2θ-range (step size = 0.03°, holding time = 10 s) using Cu K_α radiation (note that both wavelengths $\lambda(K_{\alpha1})$=1.5406 Å and $\lambda(K_{\alpha2})$=1.5443 Å were used in the intensity proportion of $I(K_{\alpha2})=I(K_{\alpha1}) = 0.5$).

2.3. Electrocatalytic activity towards OER

The electrochemical activity of the dense and macroporous Fe-P films towards OER was measured in the same three-electrode system used for electrodeposition. The outer solution of the Ag/AgCl (3M KCl) electrode was made of

0.5 M KOH. All potentials measured were converted to RHE using the following equation: E(RHE) = E(Ag—AgCl) + 0.210 + 0.059 pH. The as-prepared Fe-P samples served as the WE. Polarization curves were recorded in a N_2-saturated 1 M KOH solution by scanning the potential between 1.0 V and 2.2 V (vs. RHE) at 50 mV s^{-1}. OER tests were conducted at 25 °C. To assess catalysts stability, 25 linear sweep voltammetry (LSV) curves were run consecutively.

3. Results and discussion

3.1. Bath design, morphology and structure of dense and macroporous Fe-P films

Dense and macroporous Fe-P films were deposited from the optimized electrolyte. For the latter, PS spheres were previously self-assembled on the Au surface by electrophoresis. For the sake of comparison, macroporous films made of pure Fe were also synthesized. In this case, however, a different electrolyte (see Experimental section for details) was employed since the inclusion of P in the deposits could not be avoided when plating from the hypophosphite-containing electrolyte.

The cyclic voltammetry (CV) recorded from the Fe-P electrolyte (Figure 1) shows a cathodic wave at around -0.5 V related to protons reduction (no Fe-P deposition occurs). A tepid increase of the current density is observed from -0.8 V. In this region, both hydrogen evolution and Fe-P deposition coexists [18]. The anodic scan shows two oxidation bands. According to the CV, current densities leading to appreciable Fe-P deposition were chosen for deposition on the unpatterned surfaces.

Figure 2 shows the E-t and j-t transients, respectively, recorded during the growth of the dense and porous Fe-P films. As aforementioned, galvanostatic conditions were used (i.e., evolution of potential against time was monitored) and the overall charge was kept constant. The monitored potential values were used later to deposit the macroporous films under potentiostatic conditions. Ac-

cordingly, the dense films were plated at current densities ranging from -10 to -50 mA cm^{-2} (Figure 2a), whereas the porous films were deposited at constant potential values ranging from -0.96 to -1.1 V (Figure 2b). Notice that potentiostatic deposition onto the patterned Au surfaces was selected since the real working area (unshielded areas of the substrate) could not be precisely determined. Values close to the stabilized potential (E_s) previously recorded during the growth of dense films were applied for the deposition of the macroporous films. Nevertheless, the lowest applied potential was -0.96 V since no significant deposition was observed at less negative potentials even for long deposition times.

Figure 2a shows that the value of E_s decreases as the applied current density is made more negative. A similar trend is observed in Figure 2b. Namely, the current density shifts toward more negative values as the applied potential is decreased. The typical nucleation spike is observed in the E-t curve at the lowest applied current density. Fluctuations are also observed in the E-t transients, indicating that hydrogen co-evolution accompanies Fe-P deposition. Interestingly, these become less pronounced as the current density is made more negative. On the contrary, serrations are apparently exacerbated as the applied potential is made more negative during the growth of the macroporous films. The j-t curve corresponding to the deposition of pure Fe onto the patterned Au surface is included in Figure 2b. In this case, the applied potential was -1.2 V since Fe(II) was not efficiently discharged at less negative potentials and, therefore, complete coverage of the voids was not attained even for long deposition times.

Figure 3 shows the FE-SEM images of the dense films grown at current densities of -10, -20, -30 and -50 mA cm^{-2} and at a fixed deposition charge (Q = 20 C cm^{-2}). This resulted in deposit thicknesses ranging between 1.2 and 2.0 microns. The films show a very smooth, featureless surface at the lowest current density. The grain morphology becomes gradually visible and cracks appear upon increasing the current density. These changes in morphology are accompanied by moderate variations in the chemical composition. The deposits

contained a significant amount of P between 15 and 25 at.% P (see Table 1) within the explored window of current densities. The P/Fe ratio was seemingly the lowest at -50 mA cm^{-2}. Since intense cracking and film detachment occurred at more negative current densities, the amount of P in the films could not be decreased further. Indeed, attempts to restrict the incorporation of P in the deposits by reducing the concentration of hypophosphite in the electrolyte down to 0.025 M failed. Therefore, it was clear that soon after the incorporation of P in the deposits was enabled, P entered the deposits with considerably larger amounts. The amount of P detected by EDX and ICP-OES after full dissolution of the films in diluted nitric acid were consistent, being the differences not larger than 1.5 at.% (see Supporting Information, Table S1). The incorporation of oxygen in the deposits was also noticed, in amounts ranging from 3 at.% to 22 at.%, with no clear trend with the de-aeration time prior to plating or the P percentage in the deposits, although more negative current densities seemed to favor oxygen incorporation. This is thought to correspond to a significant increase in the pH of the solution adjacent to the cathode, which results in the precipitation of iron hydroxides on the cathode and their incorporation in the growing deposit. Nevertheless, the deposits showed a metallic luster, opposite to P-free deposits electroplated from an hypophosphite-free electrolyte, which exhibited a rough and matte surface (see Supporting Information, Fig. S1). The presence of oxygen is in agreement with previous reports on electroplated Fe-P coatings [14, 49]. Indeed, if the amounts are calculated in weight percentage, the content of oxygen in the films is between 1-10 wt.%, therefore it is moderate. The efficiency of deposition was calculated to vary between 16% and 29% as the applied current density was made more negative, in agreement with the attenuation of the fluctuations observed in the E-t transients. Current efficiency values are a bit higher than the current efficiencies reported by Sesqueira et al. for the electrodeposition of Fe-P from a different bath formulation [14]. Similar to Ni-P electrodeposition, cathode current efficiency is found to increase with the increase of the absolute value of the current density [50]. Figure 4 shows the FE-SEM images of the Fe-P macroporous films obtained through the E-t

curves shown in Figure 2b after PS spheres removal. The charge flowed during deposition was between 34 C cm^{-2} and 38 C cm^{-2}. The films display a pseudo-ordered pore arrangement, the pore size being determined by the diameter of the spheres (350 nm). Slight differences in both pore wall morphology and pore size were noticed as a function of the applied potential. The samples deposited at potentials ranging from -0.96 to -1.0 V (Figure 4a-c) showed an almost identical architecture consisting of nearly a monolayer of hemispherical pores. The occurrence of pseudo-hexagonal pore arrays as large as 250 μm^2 was observed (see Figure 4c). Meanwhile, the films obtained at more negative potentials (Figure 4d, e) showed an ill-defined pore structure, featuring discontinuities between neighboring pores and rougher pore walls. Nevertheless, high porosity remained. Incipient cracking was observed in Figure 4e, hence following the same trend with the current density/potential as the dense films.

Table 1: Fe, P and O content (in at.%) determined by EDX in the dense Fe-P films as a function of the applied current density.

j / mA cm^{-2}	at. % Fe	at. % P	at. % O
-10	72	25	3
-20	64	20	16
-30	61	22	17
-50	63	15	22

Table 2 lists the amount of Fe, P and O detected in the porous films deposited within the selected experimental conditions. The phosphorous content generally increased as the applied potential was made more negative from 6-8 at.% to 14 at.%. Notice that the P contents were lower than in the dense counterparts, which can be understood considering that the diffusion and nucleation events in confined cavities are different from those on planar substrates. More importantly, the Fe/P ratio in the films showed the reverse trend with the applied current density (overpotential) compared to the dense counterparts. It is hypothesized that the serrations observed in both the E-t and j-t curves are some-

how linked to incorporation of P in the films. Namely, the Fe/P ratio decreases as the serrations are intensified in either the E-t or j-t curves. This suggests that the evolution of hydrogen gas reduces the hypophosphite enabling the codeposition of P with Fe. For deposition on planar (unpatterned) substrates, hydrogen evolution is more pronounced at more positive current densities, whereas the opposite scenario is found when deposition takes place on confined cavities, for which the distribution of current is not homogeneous. Besides, the codeposition of higher amount of phosphorus was accompanied by a reduction in the oxygen content, as it was observed for the dense films. However, the variation did not follow a monotonic trend. Overall, the amount of oxygen was higher than in the dense counterparts. This can be partly attributed to the higher tendency toward passivation of the macroporous films, composed of thin walls, in contact with air. The porous pure Fe film obtained from a different bath showed an oxygen percentage similar to the macroporous Fe-P films with 10-14 at.% P. However, in this case the applied potential is not strictly comparable and, therefore, the bath formulation itself also plays a role in determining the Fe/O ratio.

Table 2: Fe, P and O content (in at.%) determined by EDX in the macroporous Fe-P films as a function of the deposition potential.

E / V	at. % Fe	at. % P	at. % O
-0.96	60	8	32
-0.98	57	6	37
-1.0	69	10	21
-1.05	62	12	26
-1.1	65	14	21
-1.2[1]	74	0	26

[1]Note that this sample was electrodeposited from a P-free electrolyte as detailed in the Experimental section.

Figure 5 shows a detail of the XRD patterns in the 43-46° 2θ range of some

selected dense and porous Fe-P films. The main peak of the body-centered cubic (bcc) phase of Fe, if so, appears in this angular range. The weak diffraction peak located at $2\theta = 43.6°$ is due to the holder. It is known that Fe-P produced by electrodeposition gradually changes from micro/nanocrystalline to amorphous-like by increasing the phosphorus content [51]. The boundary between a microcrystalline and a fully homogeneous amorphous structure is difficult to determine and depends on the bath formulation and electrodeposition conditions. Typically, it stands for 20 at.% P. The dense films prepared at current densities between -10 mA cm^{-2} and -30 mA cm^{-2} did not show any reflection. Besides the amorphous halo, no additional reflection that could indicate a texture effect was observed in the extended XRD patterns (see Supporting Information, Fig. S2). Meanwhile, all the porous samples did show a relatively wide (110) bcc-Fe peak always. No other peaks ascribed to intermetallic phases such as FeP, Fe_2P or Fe_3P phases were detected in the full XRD patterns. Therefore, the continuous films plated up to -30 mA cm^{-2} were amorphous-like, which makes sense considering that their P amount is beyond 20 at.% P, whereas the walls of the porous films were nanocrystalline. For the macroporous films, the position of the α-Fe reflection shifted toward higher angles as P was incorporated into the deposits. For example, a shift ca. 0.13° was observed when 12 at.% P was alloyed with Fe (compare green and blue profiles in Figure 5). This shift can be explained considering that the atomic radius of P is smaller than that of Fe, which causes a shrinkage of the unit cell [52].

3.2. Surface wettability

The wettability of the dense and macroporous Fe-P films was characterized by the sessile drop technique, using 1.5 μL of MQ quality water droplets. Figure 6 shows representative photographs of the drop profile immediately after the drop was placed onto the films' surface. The macroporous Fe-P films exhibit higher contact angles than the dense counterparts. For the latter, the values range from around 80° to 100°. For the former, the values vary between 107° and 135° (see Suporting Information, Fig. S3). Therefore, it is clear that the

porous surfaces are more hydrophobic, which is likely because the air trapped within the pores precludes their wetting. This indicates that an intermediate state between the regimes of Wenzel and Cassie-Baxter predominates in the macroporous films [53, 54]. Fluctuation of the contact angle values within the same series of samples (dense *vs.* macroporous) can be understood on the basis of their dissimilar chemical composition (P, O contents) and slightly different morphology (see for example Figure 4). In any case, the effect of porosity dominates over the chemical composition, in agreement with other works on macroporous metallic films [55].

3.3. Magnetic properties

The room temperature in-plane hysteresis loops of the dense and macroporous Fe-P films deposited at varying current densities and potentials, respectively, are shown in Figure 7. Well-defined hysteresis loops were recorded in all cases, irrespective of the P content. For the dense films, a soft-ferromagnetic behavior with coercivity (H_C) values ranging between 2 Oe and 11 Oe was observed. As expected, the saturation magnetization (M_S) decreased as the P content increased, in agreement with previous works from the literature [52]. The values of M_S are consistent, bearing in mind that M_S of bulk Fe is 217.6 emu g^{-1}. The incorporation of oxygen in the coatings can further contribute to the reduction of M_S compared to pure Fe. Actually, the hysteresis loops were normalized after dissolving the films for ICP-OES analyses, which enabled to determine the deposited mass of iron and phosphorous, but not that of oxygen. Although Fe is mostly oxidized at the outermost surface, the occurrence of either antiferromagnetic (hematite) or ferrimagnetic iron oxides with lower M_S (maghemite, magnetite) would cause a decrease of the M_S.

Compared to the dense films, saturation is reached at much higher applied fields in the macroporous analogues and the coercivity is larger. Both effects are probably due to the hindrances imposed by the reduced lateral size of the pore walls on domain wall propagation as well as the loss of the in-plane shape anisotropy [27, 56]. Again, a decrease of M_S compared to pure Fe is observed.

Remarkably, all macropous films (except pure Fe) show a similar M_S, irrespective of the P content. Both the P content and the degree of oxidation of the porous films can contribute to M_S. Since the films with lower P amount (e.g., 6-8 at.%) show also higher O at.% (see Table 2), it turns out that these films exhibit virtually the same value of M_S as the porous films with 12-14 at.% P.

3.4. Electrocatalytic activity towards OER

In spite of their hydrophobic character, it was deemed appropriate to investigate the OER performance of the macroporous Fe-P films in alkaline media and compare it to the behaviour shown by their dense counterparts. The macroporous Fe-P films are expected to be suitable candidates for OER, not only because of their chemical composition but also large surface area [57]. Remarkably, the traditional synthesis of transition metal phosphides often involves the release of the highly toxic phosphine, which is against of current precepts for green chemistry and sustainable management [45]. Moreover, the use of a polymer binder during electrode fabrication from catalyst powders is avoided here since the electrocatalyst material is directly attached to a conductive surface during electrodeposition [57, 58, 59].

Figure 8 shows the steady-state polarization curves of the dense and porous Fe-P catalysts in N_2-saturated 1 M KOH solution at a sweeping rate of 50 mV s^{-1}. Although 6 M KOH solution would be more realistic considering the current water electrolysis in industrial conditions, the selected electrolyte allows a relatively good comparative analysis. While the onset for OER is similar in both sets of samples, the kinetics is faster in the macroporous films (see inset of Figure 8a) . Given that the performance of an OER catalyst is commonly measured by the overpotential (η = E − 1.23 V) required to achieve 10 mA cm^{-2} per geometric area at ambient temperature and standard pressure, this parameter is used here to evaluate the OER activity of our Fe-P deposits. If one compares the response of the most active film within both sets of samples, η is 726 mV for the dense film electrodeposited at -50 mA cm^{-2}, whereas it decreases to 580 mV for the macroporous films deposited at -0.96 V and -0.98 V. The

lower the P content in the dense films, the higher their OER kinetics. In other words, the crystalline films performed better than their amorphous analogues. A similar trend was found in the macroporous films, although in this case all the films are crystalline. Indeed, the P-free macroporous film was as active as those films containing 6-8 at.% P. EDX analysis of the P-free macroporous film indicated the presence of a larger amount of oxygen (26 at.% P). Importantly, the reported current density values are referred to the geometric area. This means that the current densities resulting from considering the actual plated area of the macroporous films would be much higher. In any case, the η at 10 mA cm^{-2} of the outperforming macroporous Fe-P films is still around 200 mV higher than the value of commercial IrO_x (320 mV) and those reported in the literature for nanostructured Fe-P, Co-Fe-P and Ni-Fe-P based catalysts tested in 1M KOH [43, 44, 45, 57]. The fact that the here-electrodeposited Fe-P films are hydrophobic might be partly responsible for the observed modest activity. It is expected that annealing of the macroporous films at mild temperatures in vacuum might increase their hydrophilicity while triggering the crystallization of active phosphides. Further work is in progress to assess the impact of annealing over OER performance.

In electrocatalytic processes, catalysts may suffer from deformation of the structure, poisoning and thus loss of the catalytic activity. In order to examine their catalytic durability, the dense and macroporous films were subjected to 25 cycles in 1 M KOH within the potential range from +1.0 to +2.2 V. As shown in Figure 8c-d, the activity remains fairly the same after 25 linear sweep voltammetry (LSV) curves. Most importantly, inspection of the films after OER tests suggested the formation of abundant hydroxides/oxyhydroxides on the surface of the samples, as noted by the presence of leaf-like features (see Figure 9). Expectedly, the corresponding EDX analyses yielded much larger amount of oxygen than in the pristine films. For example, the EDX analysis of the dense Fe-P film gave 42 at.% O, 12 at.% P and 46 at.% Fe. The formation of FeO and FeOOH species during OER tests has been identified as the reason for the catalytic activity of transition metal phosphides [44].

4. Conclusions

Macroporous Fe-P films with varying P content (8-14 at.% P) were obtained by potentiostatic electrodeposition on colloidal crystal templates. The pore walls were nanocrystalline and showed the bcc-Fe structure. Analogous dense Fe-P films deposited galvanostatically showed larger amounts of P, enabling the formation of amorphous-like deposits. The macroporous films were more hydrophobic than their dense counterparts, which can be ascribed to the larger roughness imposed by the macroporous network rather than differences in the Fe/P ratio. In addition, these films were soft ferromagnetic. The recorded hysteresis loops indicated that the porous films were more difficult to saturate and exhibited higher coercivity values, probably due to the hindrances imposed by the pore walls on the propagation of domain walls during magnetization reversal. In spite of their hydrophobic character, both the dense and macroporous Fe-P films displayed some OER activity in alkaline media. Thanks to their porous structure and possibly lower P amounts, the OER kinetics of the macroporous films was higher than their dense counterparts. The present work indicates that Fe-P system is a versatile material whose structure can be engineered on demand by electrodeposition. The resulting coatings are interesting for diverse applications, including soft-ferromagnetic components, energy-efficient magnetoelectric actuation, magnetic refrigerators with enhanced performance, water cleaning, water splitting or combinations thereof.

Acknowledgements

This work was supported by the Spanish Government (MAT2017-86357-C3-1-R, MAT2017-86357-C3-2-R and associated FEDER projects), the European Research Council under the SPIN-PORICS 2014-Consolidator Grant (Agreement n. 648454), the Generalitat de Catalunya (2017-SGR-292) and the L'Oréal-Unesco For Women in Science programme. EP is grateful to MINECO

for the “Ramon y Cajal“ contract (RYC-2012-10839). The authors would like to acknowledge networking support by the COST Action e-MINDS MP1407.

References

[1] G. Panzeri, A. Accogli, E. Gibertini, C. Rinaldi, L. Nobili, L. Magagnin, Electrodeposition of high-purity nanostructured iron films from fe(ii) and fe(iii) non-aqueous solutions based on ethylene glycol, Electrochimica Acta 271 (2018) 576 – 581. doi:https://doi.org/10.1016/j.electacta.2018.03.174.
URL http://www.sciencedirect.com/science/article/pii/S0013468618306911

[2] A. Nicolenco, N. Tsyntsaru, H. Cesiulis, Fe (iii)-based ammonia-free bath for electrodeposition of fe-w alloys, Journal of The Electrochemical Society 164 (9) (2017) D590–D596. arXiv:http://jes.ecsdl.org/content/164/9/D590.full.pdf+html, doi:10.1149/2.1001709jes.
URL http://jes.ecsdl.org/content/164/9/D590.abstract

[3] M. Izaki, Electrodeposition of Iron and Iron Alloys, John Wiley Sons, Ltd, 2011, Ch. 11, pp. 309–326. arXiv:https://onlinelibrary.wiley.com/doi/pdf/10.1002/9780470602638.ch11, doi:10.1002/9780470602638.ch11.
URL https://onlinelibrary.wiley.com/doi/abs/10.1002/9780470602638.ch11

[4] D. V. Kumar, S. Ayyagari, M. Prasad, Mechanical characteristics and electrochemical behaviour of electrodeposited nanocrystalline iron and iron-nickel alloy, Materials Chemistry and Physics 201 (2017) 26 – 34. doi:https://doi.org/10.1016/j.matchemphys.2017.08.025.
URL http://www.sciencedirect.com/science/article/pii/S0254058417306429

[5] V. Torabinejad, M. Aliofkhazraei, S. Assareh, M. Allahyarzadeh, A. S. Rouhaghdam, Electrodeposition of ni-fe alloys, composites, and nano coatings - a review, Journal of Alloys and Compounds 691 (2017) 841 – 859. doi:https://doi.org/10.1016/j.jallcom.2016.08.329.
URL http://www.sciencedirect.com/science/article/pii/S0925838816327311

[6] E. Dislaki, J. Sort, E. Pellicer, Parametric aqueous electrodeposition study and characterization of fe-cu films, Electrochimica Acta 231 (2017) 739 – 748. doi:https://doi.org/10.1016/j.electacta.2017.02.092.
URL http://www.sciencedirect.com/science/article/pii/S0013468617303687

[7] N. Fujita, M. Inoue, K. Arai, P. B. Lim, T. Fujii, Electrochemical deposition of amorphous feb films with soft magnetic properties, Journal of Applied Physics 83 (11) (1998) 7294–7296. arXiv:https://doi.org/10.1063/1.367757, doi:10.1063/1.367757.
URL https://doi.org/10.1063/1.367757

[8] M. Izaki, N. Miyamoto, A. Nakae, T. Hasegawa, S. Watase, M. Chigane, Y. Fujiwara, M. Ishikawa, H. Enomoto, Martensitic iron-carbon-boron alloy electrodeposit with improved mechanical properties, Journal of The Electrochemical Society 149 (7) (2002) C370–C374. arXiv:http://jes.ecsdl.org/content/149/7/C370.full.pdf+html, doi:10.1149/1.1484376.
URL http://jes.ecsdl.org/content/149/7/C370.abstract

[9] T. Müller, A. Bachmaier, R. Konetschnik, T. Schöberl, R. Pippan, Mechanical properties of electrodeposited amorphous/crystalline multilayer structures in the fe-p system, Materials Science and Engineering: A 715 (2018) 83 – 91. doi:https://doi.org/10.1016/j.msea.2017.12.090.
URL http://www.sciencedirect.com/science/article/pii/S0921509317316982

[10] S. Zečević, J. Zotović, S. Gojković, V. Radmilović, Electrochemically deposited thin films of amorphous FeP alloy: Part I. chemical composition and phase structure characterization, Journal of Electroanalytical Chemistry 448 (2) (1998) 245 – 252. doi:http://dx.doi.org/10.1016/S0022-0728(97)00417-8.
URL http://www.sciencedirect.com/science/article/pii/S0022072897004178

[11] S. Vitkova, M. Kjuchukova, G. Raichevski, Electrochemical preparation of amorphous Fe-P alloys, Journal of Applied Electrochemistry 18 (5) (1988) 673 – 678. doi:10.1007/BF01016891.
URL http://dx.doi.org/10.1007/BF01016891

[12] H. J. Soares, O. S. Campos, D. F. Dias, P. N. Casciano, P. de Lima-Neto, A. N. Correia, Chemical, morphological and corrosion characterisations of electrodeposited ni-fe-p coatings, Electrochimica Acta 284 (2018) 18 – 23. doi:https://doi.org/10.1016/j.electacta.2018.07.151.
URL http://www.sciencedirect.com/science/article/pii/S0013468618316669

[13] R. Lacasse, E. Potvin, F. Allaire, G. Houlachi, J. Cave, M. Trudeau, Electroplating: An alternative for producing low magnetic loss amorphous alloys, Plating and Surface Finishing 97 (2010) 28–35.

[14] C. Sequeira, D. Santos, P. Brito, Electrocatalytic activity of simple and modified Fe-P electrodeposits for hydrogen evolution from alkaline media, Energy 36 (2) (2011) 847 – 853. doi:http://dx.doi.org/10.1016/j.energy.2010.12.030.
URL http://www.sciencedirect.com/science/article/pii/S0360544210007206

[15] T. Osaka, M. Takai, A. Nakamura, F. Asa, K. Ohashi, H. Tachibana, Preparation of electrodeposited fep films and their soft magnetic prop-

erties, Journal of the Magnetics Society of Japan 18 (1994) 187–190. doi:10.3379/jmsjmag.18.S1_187.

[16] K. Kamei, Y. Maehara, Magnetic properties and microstructure of electrodeposited FeP amorphous alloy, Journal of Applied Electrochemistry 26 (5) (1996) 529 – 535. doi:10.1007/BF01021977.
URL http://dx.doi.org/10.1007/BF01021977

[17] M. S. Chandrasekar, S. Mitra, Electrodeposition of iron phosphide on copper substrate as conversion negative electrode for lithium-ion battery application, Ionics 20 (1) (2014) 137 – 140. doi:10.1007/s11581-013-1021-z.
URL http://dx.doi.org/10.1007/s11581-013-1021-z

[18] Y. Wu, M. Han, Electrodeposited fe-p nanowire arrays in hard-anodic aluminum oxide templates with controllable magnetic properties by thermal annealing, Journal of Alloys and Compounds 688 (2016) 783 – 789. doi:https://doi.org/10.1016/j.jallcom.2016.07.251.
URL http://www.sciencedirect.com/science/article/pii/S0925838816322861

[19] A. Stein, R. C. Schroden, Colloidal crystal templating of three-dimensionally ordered macroporous solids: materials for photonics and beyond, Current Opinion in Solid State and Materials Science 5 (6) (2001) 553 – 564. doi:http://dx.doi.org/10.1016/S1359-0286(01)00022-5.
URL http://www.sciencedirect.com/science/article/pii/S1359028601000225

[20] S. A. Davis, S. L. Burkett, N. H. Mendelson, S. Mann, Bacterial templating of ordered macrostructures in silica and silica-surfactant mesophases, Nature 385 (6615) (1997) 420 – 423. doi:10.1038/385420a0.
URL http://dx.doi.org/10.1038/385420a0

[21] A. Imhof, D. J. Pine, Ordered macroporous materials by emulsion templating, Nature 389 (6654) (1997) 948 – 951. doi:10.1038/40105.
URL http://dx.doi.org/10.1038/40105

[22] J. E. G. J. Wijnhoven, W. L. Vos, Preparation of photonic crystals made of air spheres in titania, Science 281 (1998) 802 – 804.
URL http://www.sciencemag.org/content/281/5378/802

[23] P. N. Bartlett, M. A. Ghanem, I. S. El Hallag, P. de Groot, A. Zhukov, Electrochemical deposition of macroporous magnetic networks using colloidal templates, Journal of Materials Chemistry 13 (2003) 2596 – 2602. doi:10.1039/B304496C.
URL http://dx.doi.org/10.1039/B304496C

[24] P. V. Braun, P. Wiltzius, Microporous materials: Electrochemically grown photonic crystals, Nature 402 (6762) (1999) 603 – 604. doi:10.1038/45137.

[25] P. V. Braun, P. Wiltzius, Electrochemical fabrication of 3D microperiodic porous materials, Advanced Materials 13 (7) (2001) 482 – 485.

[26] C. Navarro-Senent, J. Fornell, E. Isarain-Chávez, A. Quintana, E. Menéndez, M. Foerster, L. Aballe, E. Weschke, J. Nogués, E. Pellicer, J. Sort, Large magnetoelectric effects in electrodeposited nanoporous microdisks driven by effective surface charging and magneto-ionics, ACS Applied Materials & Interfaces (2018) 44897–44905arXiv:https://doi.org/10.1021/acsami.8b17442, doi:10.1021/acsami.8b17442.
URL https://doi.org/10.1021/acsami.8b17442

[27] A. Quintana, J. Zhang, E. Isarain-Chávez, E. Menéndez, R. Cuadrado, R. Robles, M. D. Baró, M. Guerrero, S. Pané, B. J. Nelson, C. M. Müller, P. Ordejón, J. Nogués, E. Pellicer, J. Sort, Voltage-induced coercivity reduction in nanoporous alloy films: A boost toward energy-efficient magnetic actuation, Advanced Functional Materials 27 (32) (2017) 1701904. arXiv:https://onlinelibrary.wiley.com/doi/pdf/10.1002/adfm.201701904, doi:10.1002/adfm.201701904.
URL https://onlinelibrary.wiley.com/doi/abs/10.1002/adfm.201701904

[28] L. T. Quickel, Thomas E.and Schelhas, R. A. Farrell, N. Petkov, V. H. Le, S. H. Tolbert.

[29] T. Fuchigami, R. Kawamura, Y. Kitamoto, M. Nakagawa, Y. Namiki, A magnetically guided anti-cancer drug delivery system using porous fept capsules, Biomaterials 33 (5) (2012) 1682 – 1687. doi:https://doi.org/10.1016/j.biomaterials.2011.11.016.
URL http://www.sciencedirect.com/science/article/pii/S0142961211013706

[30] M. Hrubovkov, M. Kupkov, M. Dupon, Fe and fe-p foam for biodegradable bone replacement material: Morphology, corrosion behaviour, and mechanical properties, Advances in Materials Science and Engineering 2016. doi:10.1155/2016/6257368.

[31] R. D. L. Smith, M. S. Prévot, R. D. Fagan, Z. Zhang, P. A. Sedach, M. K. J. Siu, S. Trudel, C. P. Berlinguette, Photochemical route for accessing amorphous metal oxide materials for water oxidation catalysis, Science 340 (6128) (2013) 60 – 63. arXiv:http://science.sciencemag.org/content/340/6128/60.full.pdf, doi:10.1126/science.1233638.
URL http://science.sciencemag.org/content/340/6128/60

[32] T. R. Cook, D. K. Dogutan, S. Y. Reece, Y. Surendranath, T. S. Teets, D. G. Nocera, Solar energy supply and storage for the legacy and nonlegacy worlds, Chemical Reviews 110 (11) (2010) 6474 – 6502. arXiv:http://dx.doi.org/10.1021/cr100246c, doi:10.1021/cr100246c.
URL http://dx.doi.org/10.1021/cr100246c

[33] M. Carmo, D. L. Fritz, J. Mergel, D. Stolten, A comprehensive review on PEM water electrolysis, International Journal of Hydrogen Energy 38 (12) (2013) 4901 – 4934. doi:http://dx.doi.org/10.1016/j.ijhydene.2013.01.151.
URL http://www.sciencedirect.com/science/article/pii/S0360319913002607

[34] T. Reier, M. Oezaslan, P. Strasser, Electrocatalytic oxygen evolution reaction (OER) on Ru, Ir, and Pt catalysts: A comparative study of nanoparticles and bulk materials, ACS Catalysis 2 (8) (2012) 1765 – 1772. arXiv:http://dx.doi.org/10.1021/cs3003098, doi:10.1021/cs3003098.
URL http://dx.doi.org/10.1021/cs3003098

[35] M. G. Walter, E. L. Warren, J. R. McKone, S. W. Boettcher, Q. Mi, E. A. Santori, N. S. Lewis, Solar water splitting cells, Chemical Reviews 110 (11) (2010) 6446 – 6473. arXiv:http://dx.doi.org/10.1021/cr1002326, doi:10.1021/cr1002326.
URL http://dx.doi.org/10.1021/cr1002326

[36] A. Han, S. Jin, H. Chen, H. Ji, Z. Sun, P. Du, A robust hydrogen evolution catalyst based on crystalline nickel phosphide nanoflakes on three-dimensional graphene/nickel foam: high performance for electrocatalytic hydrogen production from pH 0-14, Journal of Materials Chemistry A 3 (2015) 1941 – 1946. doi:10.1039/C4TA06071G.
URL http://dx.doi.org/10.1039/C4TA06071G

[37] Y. Shi, B. Zhang, Recent advances in transition metal phosphide nanomaterials: synthesis and applications in hydrogen evolution reaction, Chemical Society Reviews 45 (2016) 1529 – 1541. doi:10.1039/C5CS00434A.
URL http://dx.doi.org/10.1039/C5CS00434A

[38] J. Wang, W. Cui, Q. Liu, Z. Xing, A. M. Asiri, X. Sun, Recent progress in cobalt-based heterogeneous catalysts for electrochemical water splitting, Advanced Materials 28 (2) (2016) 215 – 230. doi:10.1002/adma.201502696.
URL http://dx.doi.org/10.1002/adma.201502696

[39] P. Xiao, W. Chen, X. Wang, A review of phosphide-based materials for electrocatalytic hydrogen evolution, Advanced Energy Materials 5 (24) (2015) 1500985. doi:10.1002/aenm.201500985.
URL http://dx.doi.org/10.1002/aenm.201500985

[40] Z. Pu, Q. Liu, P. Jiang, A. M. Asiri, A. Y. Obaid, X. Sun, CoP nanosheet arrays supported on a Ti plate: An efficient cathode for electrochemical hydrogen evolution, Chemistry of Materials 26 (15) (2014) 4326 – 4329. arXiv:http://dx.doi.org/10.1021/cm501273s, doi:10.1021/cm501273s.
URL http://dx.doi.org/10.1021/cm501273s

[41] J. Ryu, N. Jung, J. H. Jang, H.-J. Kim, S. J. Yoo, In situ transformation of hydrogen-evolving CoP nanoparticles: Toward efficient oxygen evolution catalysts bearing dispersed morphologies with Co-oxo/hydroxo molecular units, ACS Catalysis 5 (7) (2015) 4066 – 4074. arXiv:http://dx.doi.org/10.1021/acscatal.5b00349, doi:10.1021/acscatal.5b00349.
URL http://dx.doi.org/10.1021/acscatal.5b00349

[42] L.-A. Stern, L. Feng, F. Song, X. Hu, Ni_2P as a Janus catalyst for water splitting: the oxygen evolution activity of Ni_2P nanoparticles, Energy & Environmental Science 8 (2015) 2347 – 2351. doi:10.1039/C5EE01155H.
URL http://dx.doi.org/10.1039/C5EE01155H

[43] K. Liu, C. Zhang, Y. Sun, G. Zhang, X. Shen, F. Zou, H. Zhang, Z. Wu, E. C. Wegener, C. J. Taubert, J. T. Miller, Z. Peng, Y. Zhu, High-performance transition metal phosphide alloy catalyst for oxygen evolution reaction, ACS Nano 12 (1) (2018) 158–167. doi:10.1021/acsnano.7b04646.
URL https://doi.org/10.1021/acsnano.7b04646

[44] W. Xu, S. Zhu, Y. Liang, Z. Cui, X. Yang, A. Inoue, A nanoporous metal phosphide catalyst for bifunctional water splitting, J. Mater. Chem. A 6 (2018) 5574–5579. doi:10.1039/C8TA00622A.

[45] T. Wang, C. Wang, Y. Jin, A. Sviripa, J. Liang, J. Han, Y. Huang, Q. Li, G. Wu, Amorphous co-fe-p nanospheres for efficient water oxidation, Journal of Materials Chemistry A 5 (2017) 25378–25384. doi:10.1039/C7TA08720A.

[46] J. Xu, J. Li, D. Xiong, B. Zhang, Y. Liu, K.-H. Wu, I. Amorim, W. Li, L. Liu, Trends in activity for the oxygen evolution reaction on transition metal (m = fe, co, ni) phosphide pre-catalysts, Chem. Sci. 9 (2018) 3470–3476. doi:10.1039/C7SC05033J.
URL http://dx.doi.org/10.1039/C7SC05033J

[47] J. Masud, S. Umapathi, N. Ashokaan, M. Nath, Iron phosphide nanoparticles as an efficient electrocatalyst for the oer in alkaline solution, Journal of Materials Chemistry A 4 (2016) 9750–9754. doi:10.1039/C6TA04025J.
URL http://dx.doi.org/10.1039/C6TA04025J

[48] D. Xue, H. Shi, The fabrication and characteristic properties of amorphous fe1-xPx alloy nanowire arrays, Nanotechnology 15 (12) (2004) 1752–1755. doi:10.1088/0957-4484/15/12/009.
URL https://doi.org/10.1088%2F0957-4484%2F15%2F12%2F009

[49] V. A. Safonov, O. V. Safonova, L. A. Fishgoit, K. Kvashnina, P. Glatzel, Chemical state of phosphorus in amorphous nifep electroplates, Surface and Coatings Technology 275 (2015) 239 – 244. doi:https://doi.org/10.1016/j.surfcoat.2015.05.013.
URL http://www.sciencedirect.com/science/article/pii/S0257897215300086

[50] D. A. Luke, Nickel-phosphorus electrodeposits, Transactions of the IMF 64 (1) (1986) 99–104. arXiv:https://doi.org/10.1080/00202967.1986.11870744, doi:10.1080/00202967.1986.11870744.
URL https://doi.org/10.1080/00202967.1986.11870744

[51] F. Wang, K. Itoh, T. Watanabe, Relationship between the crystallographic structure of electrodeposited Fe-P alloy film and its thermal equilibrium phase diagram, Materials Transactions 44 (1) (2003) 127 – 132. doi:10.2320/matertrans.44.127.

[52] E. P. Elsukov, Y. N. Vorobev, A. V. Trubachev, V. A. Barinov, Structure and magnetic properties of fep electrodeposited alloys,

Physica Dtatus Solidi (a) 117 (1) (1990) 291–298. arXiv:https://onlinelibrary.wiley.com/doi/pdf/10.1002/pssa.2211170131, doi:10.1002/pssa.2211170131.
URL https://onlinelibrary.wiley.com/doi/abs/10.1002/pssa.2211170131

[53] V. R. Gonçales, M. H. Gaitán, A. de O.P. Bragatto, G. J. Soler-Illia, L. M. Baraldo, S. I. C. de Torresi, Correlation between pore size and reactivity of macro/mesoporous iron and copper hexacyanoferrates for H_2O_2 electrocatalysis, Journal of Electroanalytical Chemistry 706 (2013) 48 – 54. doi:http://dx.doi.org/10.1016/j.jelechem.2013.07.029.
URL http://www.sciencedirect.com/science/article/pii/S1572665713003354

[54] C. R. Szczepanski, F. Guittard, T. Darmanin, Recent advances in the study and design of parahydrophobic surfaces: From natural examples to synthetic approaches, Advances in Colloid and Interface Science 241 (2017) 37 – 61. doi:https://doi.org/10.1016/j.cis.2017.01.002.
URL http://www.sciencedirect.com/science/article/pii/S0001868616302780

[55] E. Dislaki, J. Pokki, S. Pané, J. Sort, E. Pellicer, Fabrication of sustainable hydrophobic and oleophilic pseudo-ordered macroporous fe-cu films with tunable composition and pore size via electrodeposition through colloidal templates, Applied Materials Today 12 (2018) 1 – 8. doi:https://doi.org/10.1016/j.apmt.2018.03.007.
URL http://www.sciencedirect.com/science/article/pii/S2352940718300878

[56] S. Robbennolt, J. Fornell, A. Quintana, H. Zhang, E. Menéndez, E. Pellicer, J. Sort, Structural and magnetic properties of fexcu1x sputtered thin films electrochemically treated to create nanoporosity for high-surface-area magnetic components, ACS Applied Nano Materials 1 (4) (2018)

1675–1682. arXiv:https://doi.org/10.1021/acsanm.8b00143, doi:10.1021/acsanm.8b00143.
URL https://doi.org/10.1021/acsanm.8b00143

[57] H. Kim, S. Oh, E. Cho, H. Kwon, 3d porous cobalt–iron–phosphorus bifunctional electrocatalyst for the oxygen and hydrogen evolution reactions, ACS Sustainable Chemistry & Engineering 6 (5) (2018) 6305–6311. doi:10.1021/acssuschemeng.8b00118.
URL https://doi.org/10.1021/acssuschemeng.8b00118

[58] I. Golvano-Escobal, S. Surińach, M. D. Baró, S. Pané, J. Sort, E. Pellicer, Electrodeposition of sizeable and compositionally tunable rhodium-iron nanoparticles and their activity toward hydrogen evolution reaction, Electrochimica Acta 194 (2016) 263 – 275. doi:https://doi.org/10.1016/j.electacta.2016.02.112.
URL http://www.sciencedirect.com/science/article/pii/S0013468616303991

[59] E. Isarain-Chávez, M. D. Baró, C. Alcantara, S. Pané, J. Sort, E. Pellicer, Micelle-assisted electrodeposition of mesoporous fept smooth thin films and their electrocatalytic activity towards the hydrogen evolution reaction, ChemSusChem 11 (2) (2018) 367–375. arXiv:https://onlinelibrary.wiley.com/doi/pdf/10.1002/cssc.201701938, doi:10.1002/cssc.201701938.
URL https://onlinelibrary.wiley.com/doi/abs/10.1002/cssc.201701938

Figure captions

Figure 1. Cyclic voltammetry recorded from the optimized electrolyte on the Au surface at 50 mV s^{-1}.

Figure 2. Representative a) E-t transients recorded during the deposition of dense Fe-P films on the Au surface at the indicated current densities and b) j-t transients recorded during the deposition of Fe-P on colloidal template arrays patterned on Au at the indicated potentials. Note that the current densities reported in b) refer to the geometric surface area of the cathode.

Figure 3. Low and high (inserts) magnification FE-SEM images of the dense Fe-P films obtained at different current densities: a) j = -10 mA cm^{-2}, b) j = -20 mA cm^{-2}, c) j = -30 mA cm^{-2}, and d) j = -50 mA cm^{-2}. The scale bars indicated in a) apply to b)-d).

Figure 4. Low and high (inserts) magnification FE-SEM images of the macroporous Fe-P films obtained at different deposition potentials: a) E = -0.96 V, b) E = -0.98 V, c) E = -1.0 V, d) E = -1.05 V and e) E = -1.1 V. f) FE-SEM image of a P-free Fe macroporous film deposited at E = -1.2 V. The PS spheres were removed prior to the imaging. The scale bars indicated in a) apply to b)-f).

Figure 5. Zoomed detail of the XRD patterns in the 43°-46° 2θ range of selected samples (with the percentage of P indicated). The peak marked with an asterisk belongs to the holder. 'd.' and 'p.' stand for dense and porous films, respectively.

Figure 6. Photographs of the MQ-water droplets on the surface of a) dense Fe-P film obtained at j = -50 mA cm^{-2} and b) macroporous Fe-P film obtained at E = -1.1 V.

Figure 7. Room temperature hysteresis loops of a) dense Fe-P films prepared at the indicated current densities and b) macroporous Fe-P films prepared at the indicated potentials. The inset in b) shows a magnified detail at low fields. The percentage of P is also given.

Figure 8. Steady-state polarization curves recorded in Ar-saturated 1 M

KOH electrolyte for a) dense and b) macroporous Fe-P films. The response of a macroporous pure Fe film is shown for comparison in b). Scan rate: 50 mV s^{-1}. The inset in a) shows the Tafel slopes for the dense film fabricated at -50 mA cm^{-2} and the porous film fabricated at -1.05 V. c) and d) show the cyclability of the same films.

Figure 9. SEM images of the surface appearance after OER cycling for a) dense Fe-P film electrodeposited at -50 mA cm^{-2} and b) macroporous Fe-P film electrodeposited at -0.96 V.

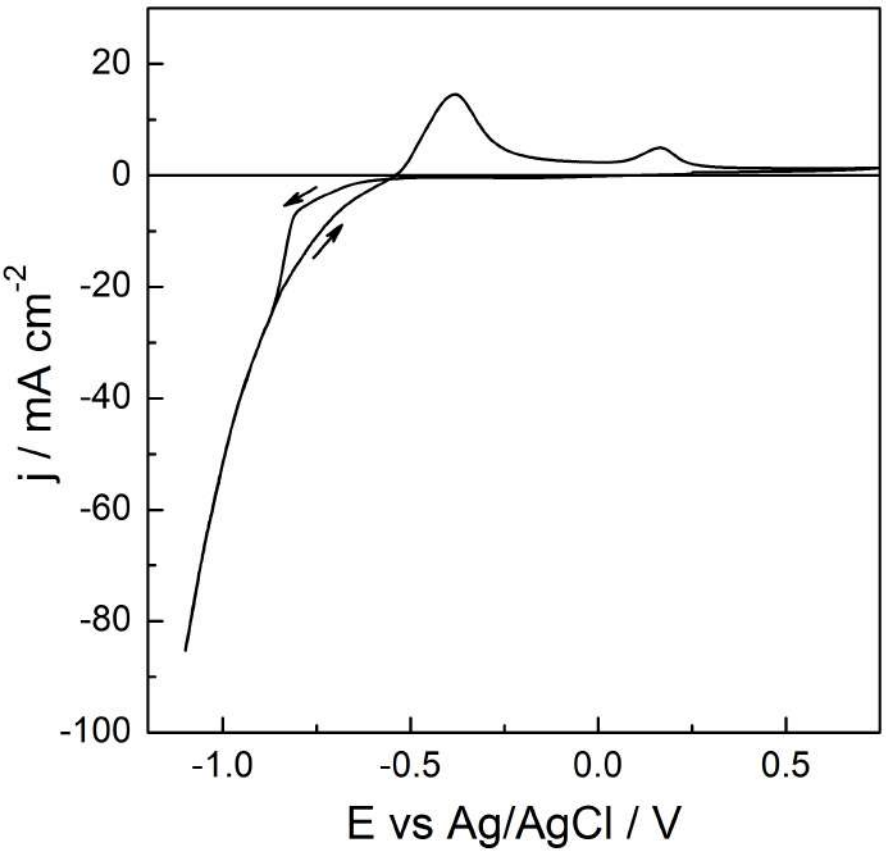

Figure 1:

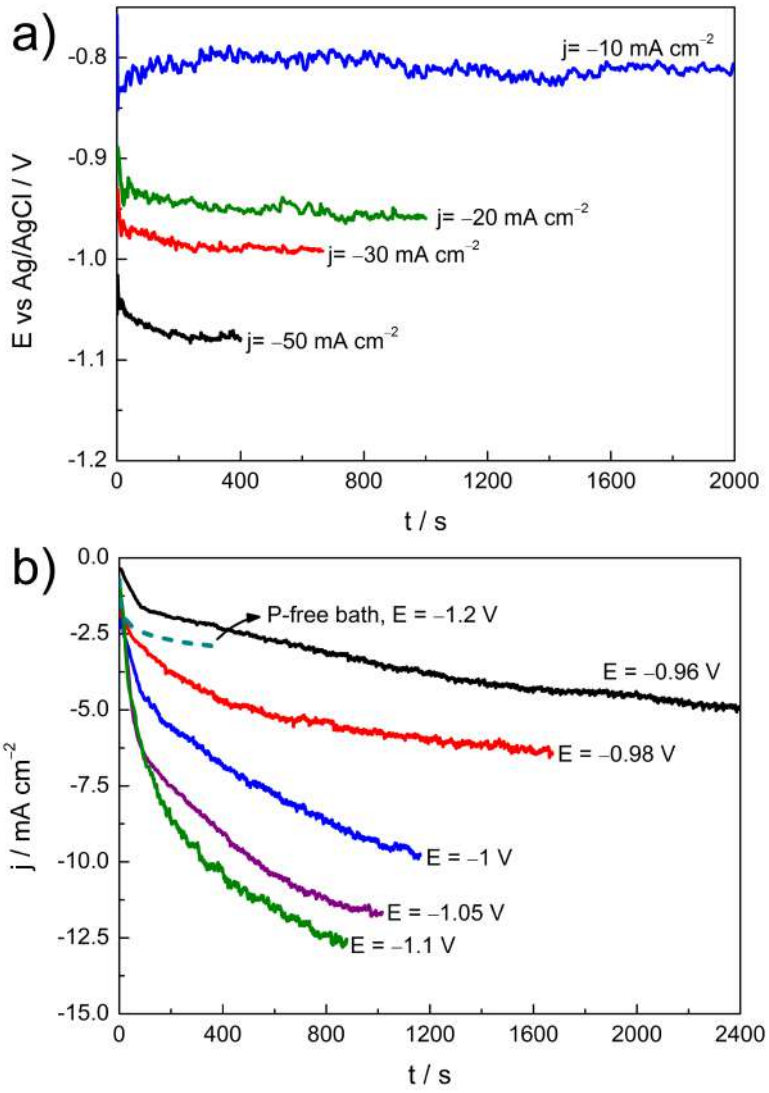
a)
-0.8
-0.9
-1.0
-1.1
-1.2
E vs Ag/AgCl / V
j= –10 mA cm^{-2}
j= –20 mA cm^{-2}
j= –30 mA cm^{-2}
j= –50 mA cm^{-2}
0
400
800
1200
1600
2000
t / s
b)
0.0
-2.5
-5.0
-7.5
-10.0
-12.5
-15.0
j / mA cm^{-2}
P-free bath, E = –1.2 V
E = –0.96 V
E = –0.98 V
E = –1 V
E = –1.05 V
E = –1.1 V
0
400
800
1200
1600
2000
2400
t / s

Figure 2:

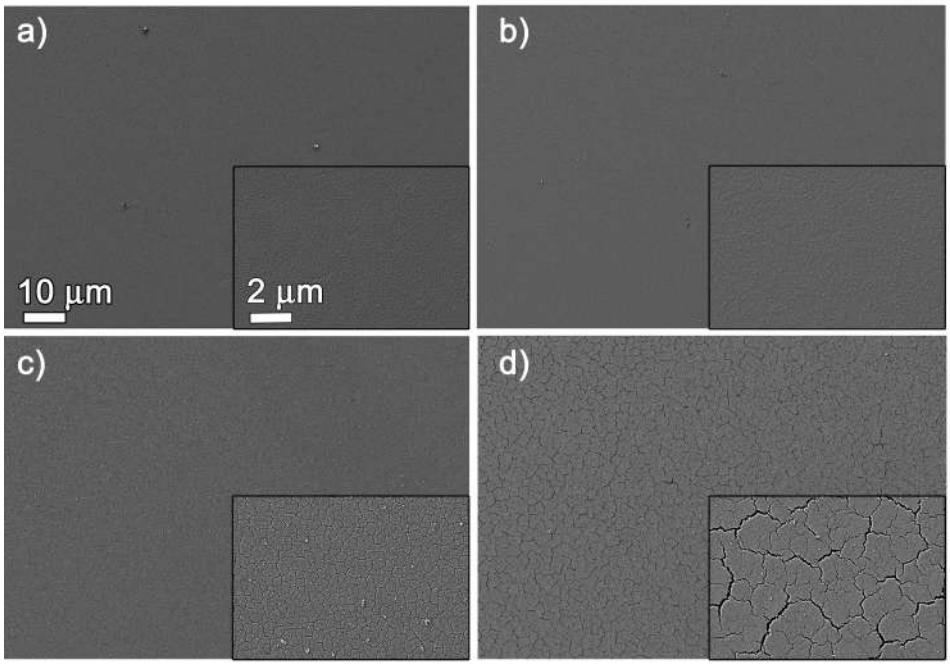

Figure 3:

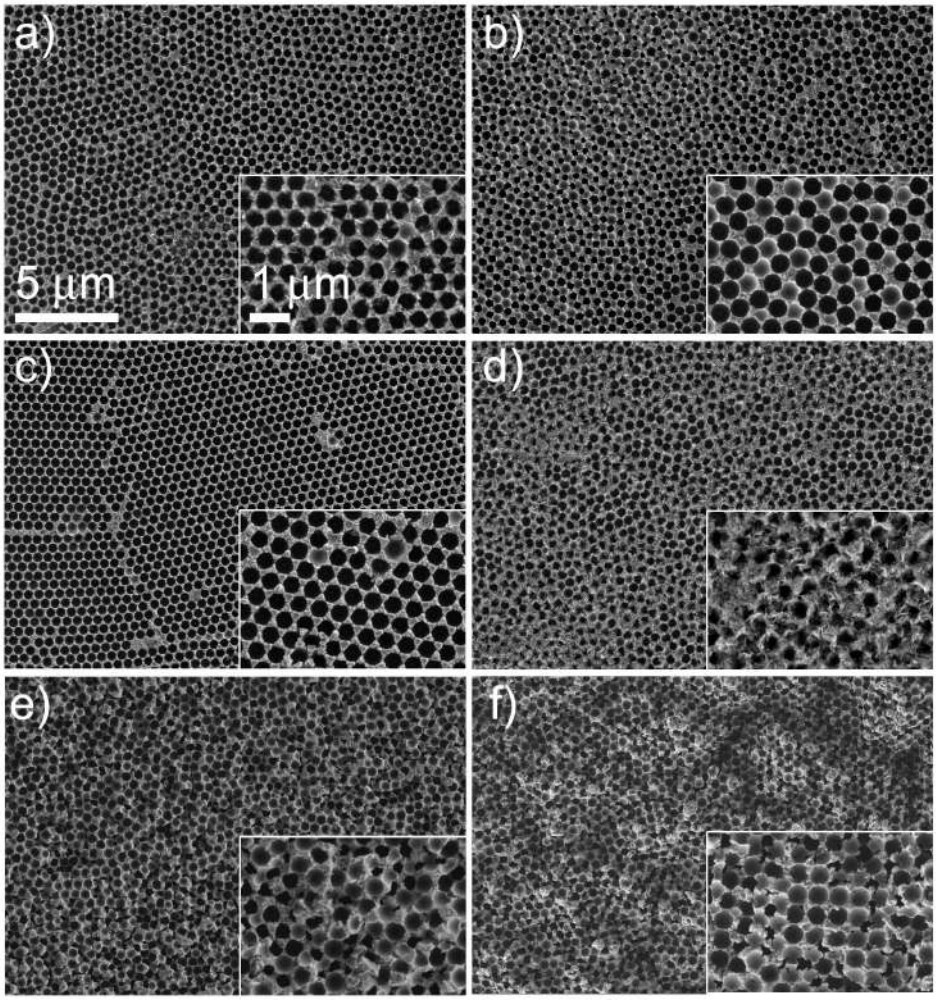

Figure 4:

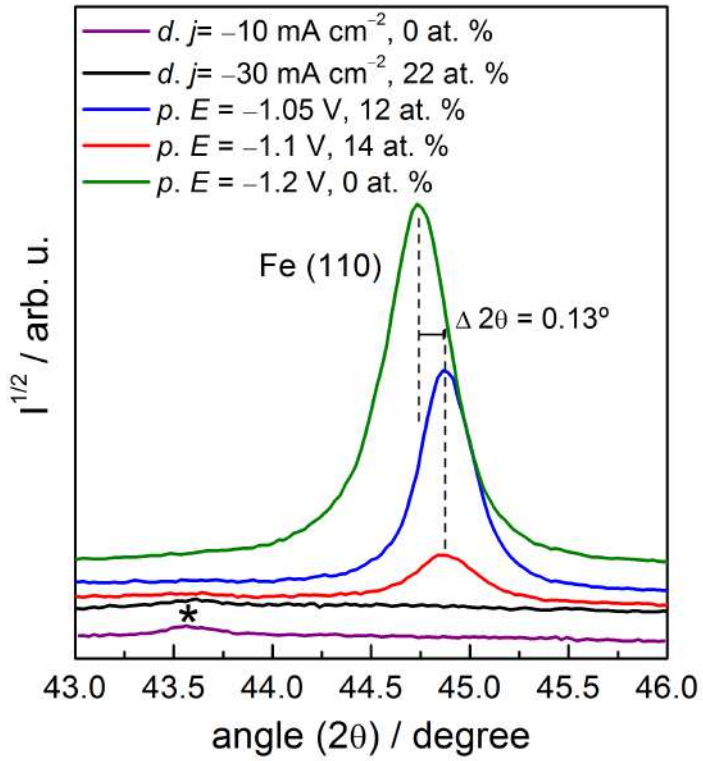
d. j= –10 mA cm^{-2}, 0 at. %
d. j= –30 mA cm^{-2}, 22 at. %
p. E = –1.05 V, 12 at. %
p. E = –1.1 V, 14 at. %
p. E = –1.2 V, 0 at. %
Fe (110)
Δ 2θ = 0.13°
*
I$^{1/2}$ / arb. u.
43.0
43.5
44.0
44.5
45.0
45.5
46.0
angle (2θ) / degree

Figure 5:

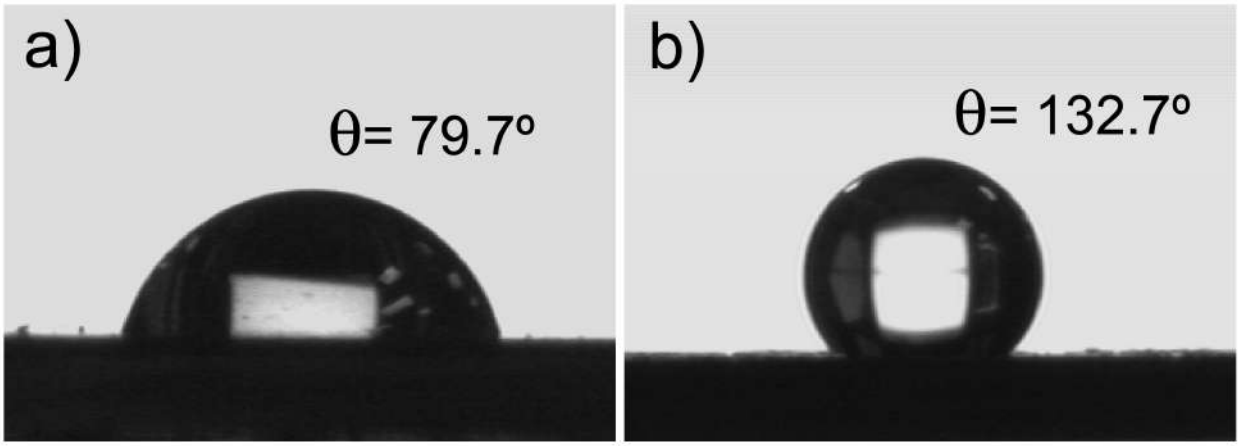

Figure 6:

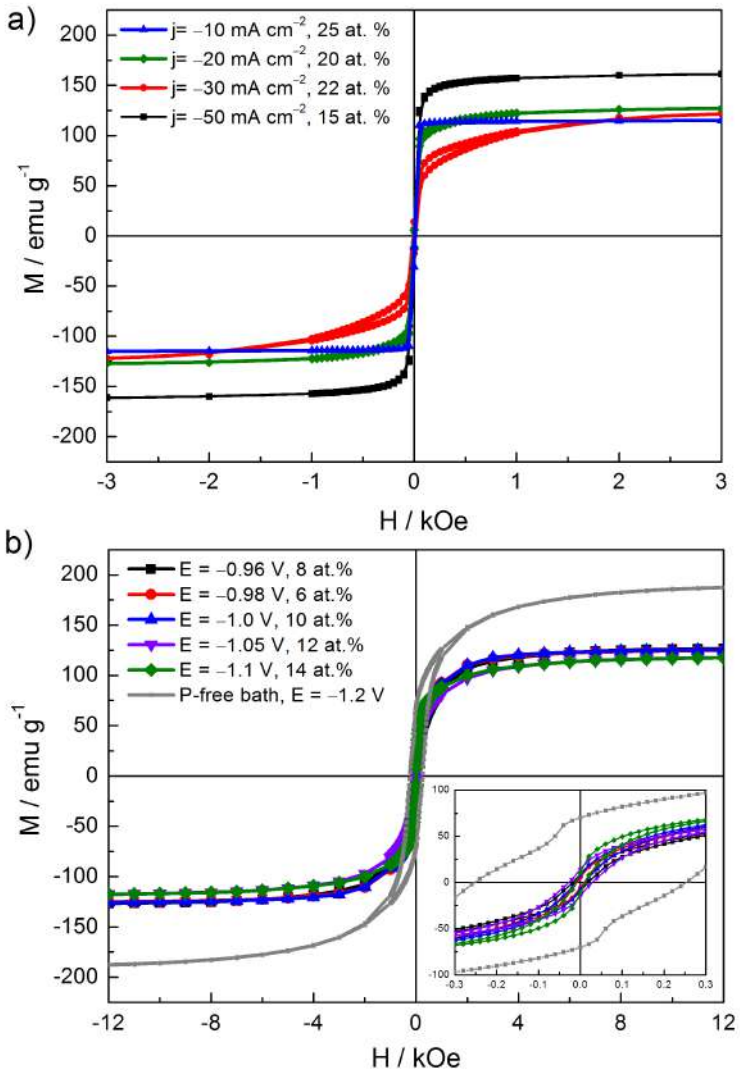
a)
j= –10 mA cm^{-2}, 25 at. %
j= –20 mA cm^{-2}, 20 at. %
j= –30 mA cm^{-2}, 22 at. %
j= –50 mA cm^{-2}, 15 at. %
M / emu g^{-1}
H / kOe
b)
E = –0.96 V, 8 at.%
E = –0.98 V, 6 at.%
E = –1.0 V, 10 at.%
E = –1.05 V, 12 at.%
E = –1.1 V, 14 at.%
P-free bath, E = –1.2 V
M / emu g^{-1}
H / kOe

Figure 7:

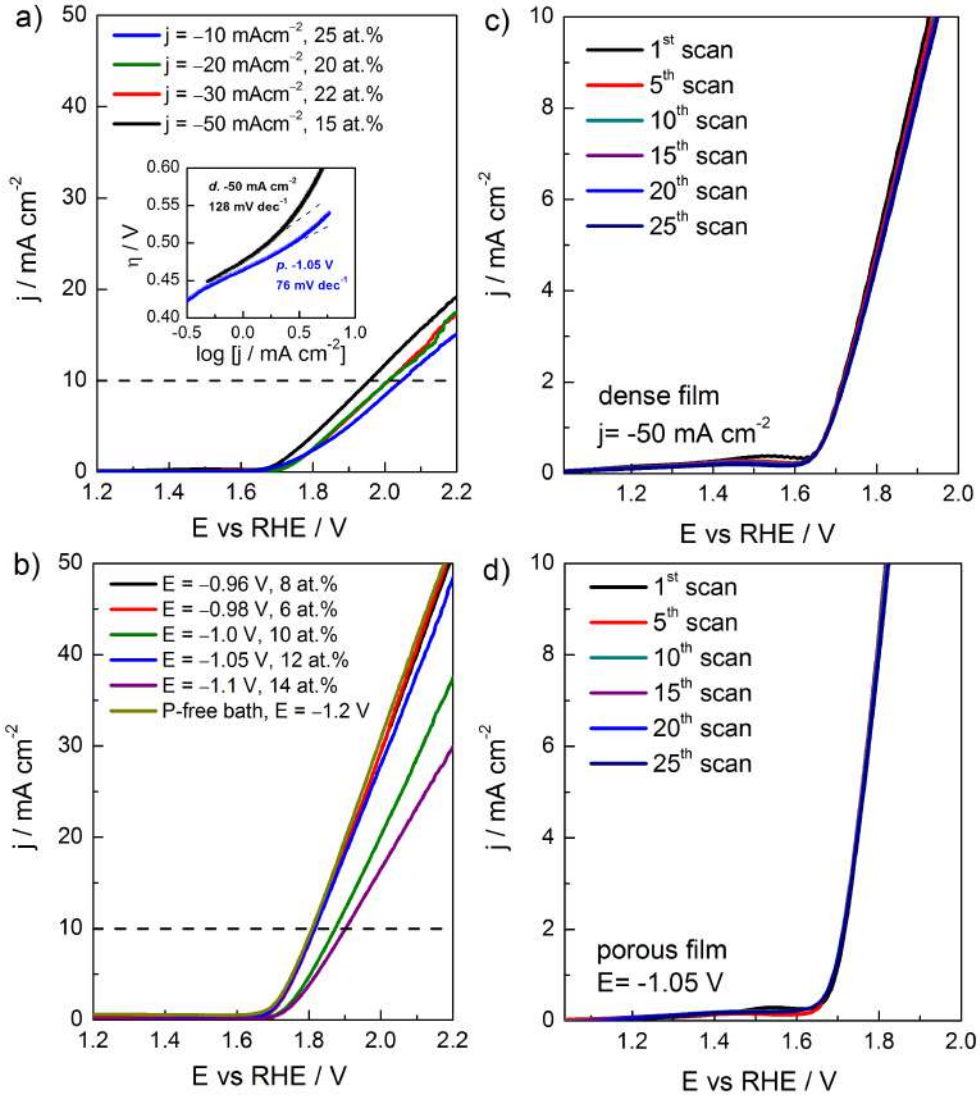
a)
j = –10 mAcm^{-2}, 25 at.%
j = –20 mAcm^{-2}, 20 at.%
j = –30 mAcm^{-2}, 22 at.%
j = –50 mAcm^{-2}, 15 at.%
d. -50 mA cm^{-2}
128 mV dec^{-1}
p. -1.05 V
76 mV dec^{-1}
η / V
log [j / mA cm^{-2}]
j / mA cm^{-2}
E vs RHE / V
b)
E = –0.96 V, 8 at.%
E = –0.98 V, 6 at.%
E = –1.0 V, 10 at.%
E = –1.05 V, 12 at.%
E = –1.1 V, 14 at.%
P-free bath, E = –1.2 V
j / mA cm^{-2}
E vs RHE / V
c)
1st scan
5th scan
10th scan
15th scan
20th scan
25th scan
dense film
j= -50 mA cm^{-2}
j / mA cm^{-2}
E vs RHE / V
d)
1st scan
5th scan
10th scan
15th scan
20th scan
25th scan
porous film
E= -1.05 V
j / mA cm^{-2}
E vs RHE / V

Figure 8:

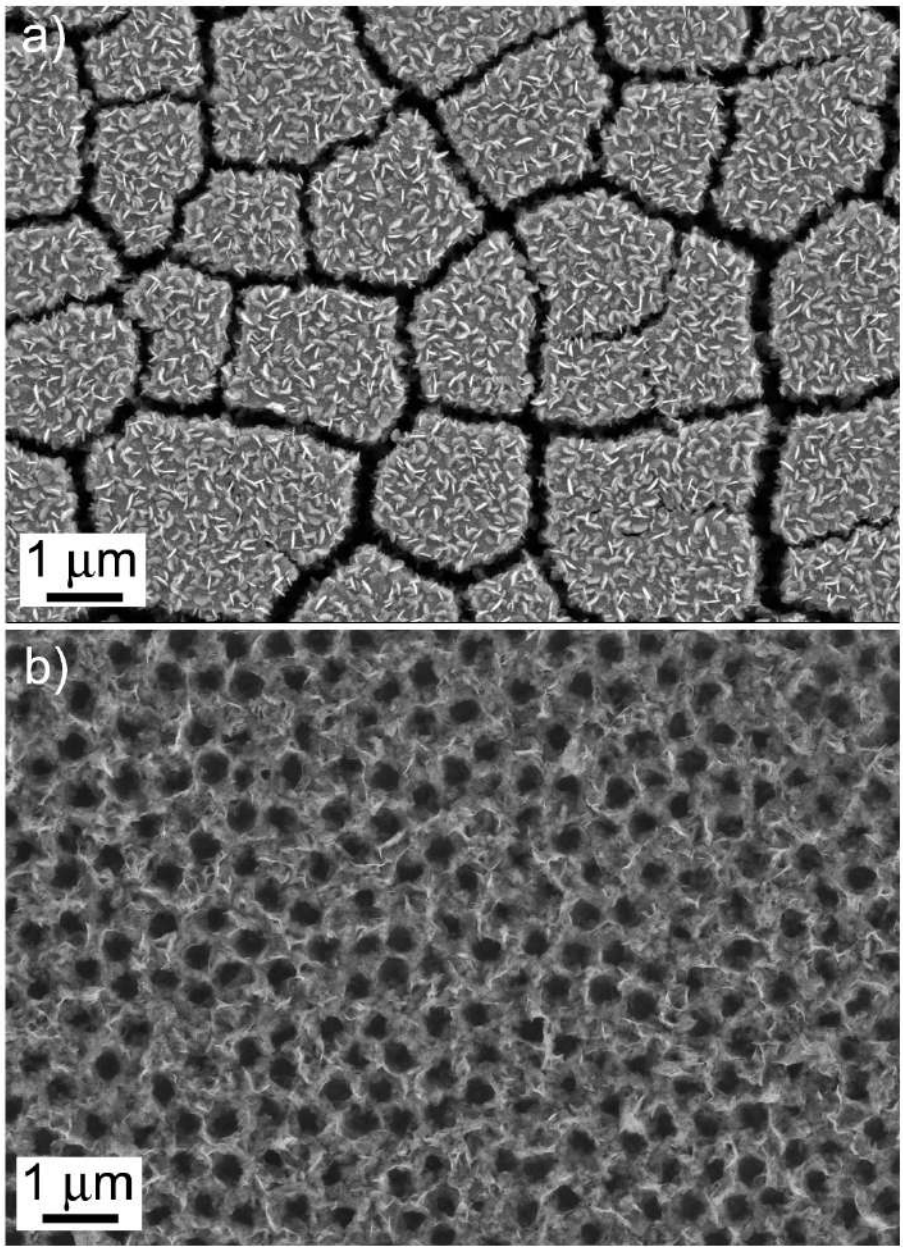

Figure 9: